

## Article

# Photocatalytic Degradation of Tetracycline by La-Fe Co-Doped SrTiO<sub>3</sub>/TiO<sub>2</sub> Composites: Performance and Mechanism Study

Mingzhu Hu <sup>1</sup>, Weifang Chen <sup>1,\*</sup> and Jie Wang <sup>2</sup>

<sup>1</sup> School of Environment and Architecture, University of Shanghai for Science and Technology, Shanghai 200093, China; 212292128@st.usst.edu.cn

<sup>2</sup> Fishery Machinery and Instrument Research Institute, Chinese Academy of Fishery Sciences, Shanghai 200092, China; wangjie@fmiri.ac.cn

\* Correspondence: chenweifang@usst.edu.cn

**Abstract:** Human health, as well as the ecosystem's natural equilibrium, may be jeopardized by the discharge of tetracycline into the aquatic environment. In order to effectively photocatalyze the degradation of tetracycline in aqueous solution under visible light, this study used a two-step hydrothermal approach to produce composites of SrTiO<sub>3</sub>/TiO<sub>2</sub> doped with two metal elements, lanthanum (La) and iron (Fe). The crystal structure, morphology, electronic structure, particle size, specific surface area and photocatalytic properties of the catalysts were assessed using a variety of methods, such as fluorescence spectroscopy, UV-Vis diffuse reflectance, X-ray diffraction, scanning electron microscopy, BET and particle size analysis. After 120 min of exposure to visible light, the co-doped catalyst showed a degradation rate of 99.1%, which was nine times greater than that of SrTiO<sub>3</sub>/TiO<sub>2</sub> at catalyst dosing of 1.6 g/L and tetracycline concentration of 20 mg/L. The synthesized photocatalyst exhibited good tolerance to changes in pH, with the degradation efficiency of tetracycline remaining stable within the pH range of 4–10. The La-Sr (Ti-Fe) O<sub>3</sub>/TiO<sub>2</sub> catalyst also demonstrated excellent photostability after recycling. The mechanism of tetracycline degradation is primarily attributed to the active oxidation by photogenerated holes and •O<sub>2</sub><sup>-</sup>. Furthermore, tetracycline degradation pathways were analyzed via HPLC-MS to identify intermediates.

**Keywords:** tetracycline; SrTiO<sub>3</sub>/TiO<sub>2</sub>; hydrothermal; photocatalytic; double dopant



**Citation:** Hu, M.; Chen, W.; Wang, J. Photocatalytic Degradation of Tetracycline by La-Fe Co-Doped SrTiO<sub>3</sub>/TiO<sub>2</sub> Composites: Performance and Mechanism Study. *Water* **2024**, *16*, 210. <https://doi.org/10.3390/w16020210>

Academic Editor: Laura Bulgariu

Received: 9 December 2023

Revised: 3 January 2024

Accepted: 5 January 2024

Published: 7 January 2024



**Copyright:** © 2024 by the authors. Licensee MDPI, Basel, Switzerland. This article is an open access article distributed under the terms and conditions of the Creative Commons Attribution (CC BY) license (<https://creativecommons.org/licenses/by/4.0/>).

## 1. Introduction

Tetracycline is a broad-spectrum antibiotic and is widely used in medicine and agriculture [1,2]. A significant amount of tetracycline was found to enter into the environment due to improper disposal of medical waste and overuse of antibiotics in the aquaculture industry [3,4]. The introduction of tetracycline into aquaculture water impacted the growth of microorganisms [5]. It was also found to be absorbed by plants and animals [5,6]. Studies have shown that tetracycline in the environment could, in turn, enter the human body through the food chain and ultimately cause the presence of antibiotic-resistant bacteria in the human body, causing harmful infections [7].

Numerous scholars have conducted extensive research to treat tetracycline, utilizing techniques like oxidation, advanced oxidation [8,9], adsorption [10], photocatalysis [7], ion exchange [11] and biodegradation [12]. Owing to its cost-effectiveness, efficiency, and eco-friendly characteristics, photocatalysis holds great promise as a technology for decomposing water, converting CO<sub>2</sub>, and degrading water pollutants [13–15]. In recent years, photocatalytic technology has witnessed a significant increase in research attention, with researchers dedicating substantial efforts towards the advancement of perovskite semiconductor oxide photocatalysts [16]. Strontium titanate (SrTiO<sub>3</sub>) offers several advantages, including easy defect modulation and excellent physicochemical stability, among other perovskite oxides. Additionally, it can be combined with TiO<sub>2</sub> to create a heterojunction-type photocatalyst [17]. Using an in situ hydrothermal process, Cao et al. [18] synthesized

SrTiO<sub>3</sub>-TiO<sub>2</sub> heterostructure nanofibers from TiO<sub>2</sub> nanofibers. When Rhodamine B was broken down in the presence of ultraviolet light, pure TiO<sub>2</sub> nanofibers exhibited less photocatalytic activity. Wei et al. [19] constructed a SrTiO<sub>3</sub>-TiO<sub>2</sub> non-homogeneous structure to enhance solar water decomposition. However, it was found that the catalytic activity of SrTiO<sub>3</sub>-TiO<sub>2</sub> alone was relatively low under photocatalytic conditions [20]. Therefore, researchers have sought ways to further improve its ability. For instance, metals such as Bi [21], Pt [22], Ag [23] and La [24] have all been loaded to SrTiO<sub>3</sub> to further enhance the photocatalytic activity. Srivastava et al. [25] revealed that after La doping, the photocatalytic activity of SrTiO<sub>3</sub> was enhanced 1.38 times that of the original. In addition, transition metals like Fe were of experimental interest due to their special electronic properties [26]. Energy level Fe<sup>3+</sup> (ionic radius 0.645 Å) is close to that of Ti<sup>4+</sup> (ionic radius 0.605 Å) [27], and Fe can act as an inhibitor of electron-hole pair recombination [28]. Thus, it is of research interest to investigate whether the incorporation of Fe and TiO<sub>2</sub> into La-SrTiO<sub>3</sub> will result in a 'double promotion' effect.

This paper focused on the synthesis of SrTiO<sub>3</sub>/TiO<sub>2</sub> composites through the hydrothermal reaction of P25 and Sr(NO<sub>3</sub>)<sub>2</sub>. Additionally, La single-metal doping and La/Fe double-metal doping of SrTiO<sub>3</sub>/TiO<sub>2</sub> were performed. The microstructures and photocatalytic properties of the composites and doped materials were investigated using various characterization techniques. In order to assess photocatalytic performance, tetracycline degradation under visible light was measured. The study investigated the effects of various factors, including catalyst dosing, initial concentration of tetracycline, pH, and coexisting substances, on the photocatalytic effect. Additionally, the cyclic stability of the catalysts was examined. Additionally, the photocatalytic mechanism was explored through active substance capture experiments. Finally, the photodegradation pathway of tetracycline has been identified through the identification of intermediate products.

## 2. Materials and Methods

### 2.1. Materials

TiO<sub>2</sub> (P25, anatase: rutile = 8:2), strontium nitrate (Sr(NO<sub>3</sub>)<sub>2</sub>), lanthanum nitrate (La(NO<sub>3</sub>)<sub>3</sub>·6H<sub>2</sub>O), ferric nitrate (Fe(NO<sub>3</sub>)<sub>3</sub>·9H<sub>2</sub>O), tetracycline, anhydrous ethanol, sodium chloride (NaCl), sodium bicarbonate (NaHCO<sub>3</sub>), disodium hydrogen phosphate (Na<sub>2</sub>HPO<sub>4</sub>), sodium sulfate (Na<sub>2</sub>SO<sub>4</sub>), sodium nitrite (NaNO<sub>2</sub>), humic acid (HA), trolamine (TEA), tert-Butanol (TBA), and 1,4-Benzoquinone (BQ) were purchased from Sinopharm Co., LTD. None of the reagents were further purified.

### 2.2. Synthesis of Photocatalysts

#### 2.2.1. Preparation of SrTiO<sub>3</sub>/TiO<sub>2</sub>

In this study, 0.1 g of P25 was added to 20 mL of strontium nitrate solution with a concentration of 0.019 mol/L. The mixture was thoroughly stirred for 30 min and then transferred to a high-pressure reactor lined with polytetrafluoroethylene. The reactor was heated in an oven at 160 °C for 8 h. The reactor was taken out of the oven and allowed sufficient time to cool to room temperature. Afterwards, the remaining mixture was cleansed with distilled water several times and dried at 60 °C. The resultant product was designated as S/TO.

#### 2.2.2. Preparation of La-SrTiO<sub>3</sub>/TiO<sub>2</sub>

Then, 0.1 g of S/TO was added to 20 mL of 0.01 mol/L lanthanum nitrate solution and stirred for 30 min. The pH of the mixture was adjusted to 12 with 1.0 mol/L NaOH and transferred to a reactor lined with polytetrafluoroethylene. The reactor was heated in an oven at 150 °C for 24 h before being taken out and cooled down to room temperature. The mixture was also cleansed with distilled water and dried at 60 °C for 12 h. The resultant product was a single doped composite and labelled as La-S/TO.

### 2.2.3. Preparation of La-Sr (Ti-Fe) O<sub>3</sub>/TiO<sub>2</sub>

Then, 0.1 g of S/TO was fully mixed with 20 mL of lanthanum nitrate (concentration of 0.01 mol/L) for 30 min. Following this, 10 mL of ferric nitrate solution at a concentration of 0.0037 mol/L was added and stirred for another 30 min. The pH of the solution was adjusted to 12.0, and the subsequent steps were identical to those carried out for La-S/TO. The resulting material was identified as La-S(T-Fe)/TO.

### 2.3. Characterization

The crystal structures of the prepared photocatalysts were analyzed via a Rigaku Ultima IV X-ray diffractometer (XRD) (Nippon Institute of Science, Tokyo, Japan). The equipment utilized Cu K $\alpha$  target ( $\lambda = 0.154$  nm), 40 mA, and a tube voltage of 40 kV with a scanning range of 20° to 80°. The particle size and morphology of the sample were observed by a ZEISS Gemini 300 scanning electron microscope (SEM) (Carl Zeiss, Jena, Germany). At the same time, Thermo Scientific K-Alpha X-ray photoelectron spectroscopy (XPS), Lamada950 UV visible diffuse reflectance spectroscopy (UV-vis DRS), and FLS1000 photoluminescence spectroscopy (PL) (Edinburgh Tech comp Europe Ltd., Edinburgh, Scotland) were also used to detect the surface composition, chemical valence, UV visible absorption, and fluorescence emission spectra of the photocatalyst. Catalyst-specific surface area and particle size distribution were analyzed by the Brunner-Emmett-Taylor (BET) (Mike 2460) method and Malvern Zetasizer Nano ZS90 (DLS).

### 2.4. Evaluation of Photocatalytic Performance

The photocatalytic reaction was conducted using a photochemical reaction device (BXU034, Guangzhou Xingchuang Electronics Co., Ltd., Guangzhou, China). A mercury lamp equipped with a filter to remove UV short-wave light (wavelength less than 420 nm) was utilized to obtain visible light as the light source. A quartz tube containing 25 mL of 30 mg/L tetracycline solution was added with 0.02 g of P25, S/TO, La-S/TO or La-S(T-Fe)/TO. The catalysts and tetracycline solution were well combined and left in the dark for 30 min before the light was turned on to avoid errors caused by adsorption. The reaction time for photocatalysis was set at 20, 40, 60, 80, 100 and 120 min. After a predetermined time, the sample was centrifuged, and the absorbance of the supernatant was taken into account at 357 nm. The absorbance was then used to figure out the tetracycline degradation rate.

### 2.5. Evaluation of Influencing Factors

Investigations were conducted into the effects of dosage, at the start tetracycline concentration, initial pH, and coexisting humic acid and ions on photocatalytic degradation. The initial tetracycline concentrations were between 20 and 60 mg/L, and the dosage varied from 0.4 to 2.0 g/L. The initial pH of the tetracycline solution were set at 4, 6, 8, and 10, respectively. Coexisting ions were Cl<sup>-</sup>, SO<sub>4</sub><sup>2-</sup>, CO<sub>3</sub><sup>2-</sup>/HCO<sub>3</sub><sup>-</sup>, NO<sub>2</sub><sup>-</sup>, HPO<sub>4</sub><sup>2-</sup>/PO<sub>4</sub><sup>3-</sup>, each with a concentration of 10 mmol/L, while humic acid was 30 mg/L. Photocatalytic performance under different conditions was carried out as shown in Section 2.4.

### 2.6. Tests for Stability and Evaluation of Radicals Via Quenching

First, 0.02 g of photocatalyst was added to 4 quartz tubes. A 25 mL solution containing 20 mg/L of tetracycline was added. The tubes were placed in the photochemical reactor. After the reaction, 1 mmol/L triethanolamine (TEA), tert-butanol (TBA), and p-benzoquinone (BQ) were added to the three sets of catalysts, respectively, leaving one set as the control group. All experimental steps were the same as in Section 2.4, except for the addition of the respective capturing agents.

### 2.7. Determination of Tetracycline Degradation Products

Samples were collected at various time intervals (0 min, 60 min, and 120 min) during the photocatalytic reaction process and subsequently filtered through a 0.22  $\mu$  m membrane. The Agilent UPLC1290-QTOF6550 high-performance liquid chromatography–mass

spectrometer (HPLC-MS) was utilized, along with a mobile phase that consisted of a 0.1% formic acid solution mixed with methanol, running at a rate of 0.25 mL/min. There was 5.0  $\mu$ L of injection volume. The auxiliary gas was adjusted at 8 Arb, and the sheath gas to 40 Arb. While the probe heating temperature was set to 350.00  $^{\circ}$ C, the capillary temperature was kept at 300.00  $^{\circ}$ C. The spray voltage equated to 3200 V. The water products were determined by employing a wavelength range from 190 to 400 nm.

### 3. Results and Discussion

#### 3.1. Characterization of Photocatalysts

Figure 1a illustrates the X-ray diffraction patterns of P25, S/TO, La-S/TO, and La-S(T-Fe)/TO. The XRD pattern of P25 was compared to the standard card (PDF No. 21-1272). The anatase phase of P25 was identified with six distinct diffraction peaks appearing at  $2\theta = 25.1^{\circ}$ ,  $37.4^{\circ}$ ,  $48.2^{\circ}$ ,  $54.1^{\circ}$ ,  $55.0^{\circ}$ , and  $62.8^{\circ}$ . Following the hydrothermal reaction, five additional diffraction peaks are present at  $2\theta$  angles of  $32.2^{\circ}$ ,  $39.8^{\circ}$ ,  $46.5^{\circ}$ ,  $57.7^{\circ}$ , and  $67.8^{\circ}$ , in addition to the original peaks for P25. A comparison of these peaks with the standard reference card for SrTiO<sub>3</sub> (PDF No. 35-0734) indicates a reliable match, thus confirming the formation of the SrTiO<sub>3</sub> lattice from strontium nitrate and P25 after the hydrothermal reaction. There are not many noticeable aberrations when La is added to the SrTiO<sub>3</sub> lattice. This is due to the extremely tiny difference between the lanthanum ion's (1.17  $\text{\AA}$ ) and strontium ion's (1.18  $\text{\AA}$ ) radii. Observations of the distinctive peaks of lanthanum show that the doping into the lattice was successful. This was subsequently doped with Fe, but its characteristic peaks are not observable in Figure 1a, which is probably due to too little Fe doping. Figure 1b displays the local magnified XRD, indicating that the diffraction peaks of the doped samples are weakened and shifted towards decreasing  $2\theta$ . When La<sup>3+</sup> is used as a dopant in the SrTiO<sub>3</sub> lattice, a significant amount of electrons is transferred to the CB [29]. In order to minimize energy, the position of the conduction band is lowered, resulting in volume deformations [30]. This results in a shift of the peak of the photocatalyst towards decreasing  $2\theta$ .

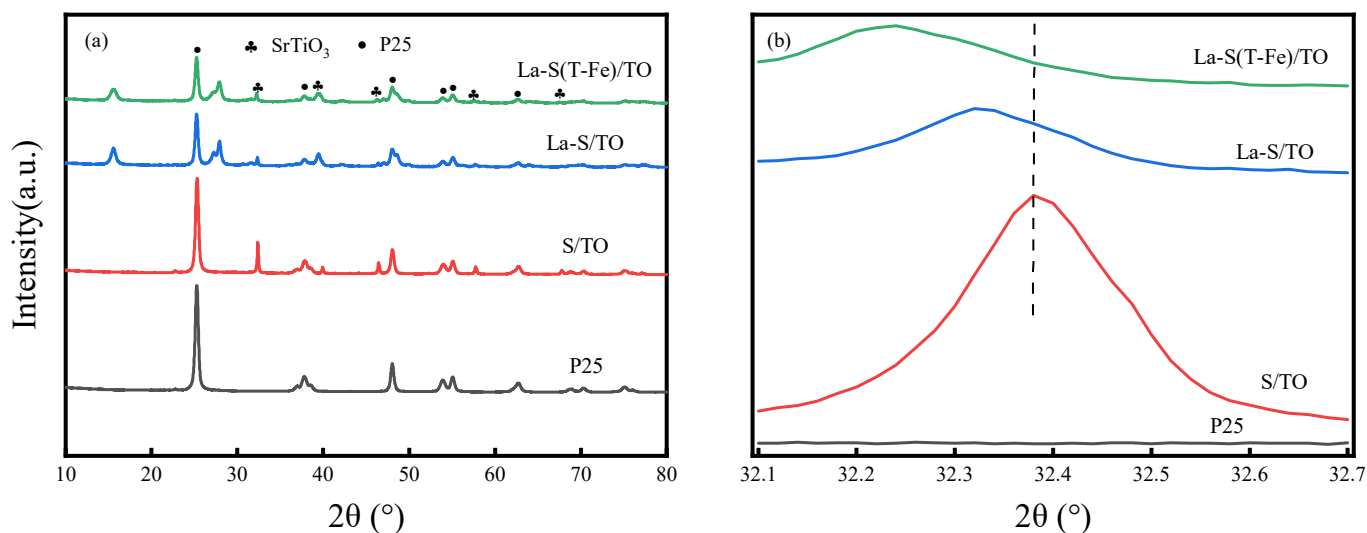


**Figure 1.** XRD analysis of catalysts: (a) XRD patterns; (b) expanded view of XRD patterns.

As shown in Figure S1, the N<sub>2</sub> absorption and desorption curve of the La-S(T-Fe)/TO catalyst corresponds to the type IV isotherm of the H3 hysteresis loop. This indicates that the pore structure of the material is very irregular and produces aggregates with a laminar structure. La-S(T-Fe)/TO has two pore sizes: mesoporous and macropores [31]. Figure S1 shows that the pore size range is primarily concentrated between 10 and 35 nm, suggesting the presence of mesoporous pores. Compared to P25, La-S(T-Fe)/TO has a larger specific surface area ( $S_{\text{BET}}$ ) and pore volume (PV) (Table 1). The enhancement of the

$S_{\text{BET}}$  augments the active sites of the catalyst, thereby improving the photocatalytic activity. Table 1 shows that the doping of La and Fe results in a significant increase in the average particle size of the material. However, the large La-S(T-Fe)/TO pore volume, as well as the pore size, mainly concentrated in the mesopore range of 10–35 nm (Figure S1), facilitates the oxidation of pollutants [32]. As a result, the internal structure of the catalyst affects how well pollutants are degraded by catalysts in addition to the catalyst's particle size.

**Table 1.** Average particle size and BET-specific surface areas of catalysts.

Sample	Average Particle Size (nm)	BET-Specific Surface Areas ( $\text{m}^2/\text{g}$ )	Pore Volume ( $\text{cm}^3/\text{g}$ )
P25	21	50	0.18
S/TO	433.9	63.3	0.33
La-S/TO	569.7	57.6	0.40
La-S(T-Fe)/TO	444.8	62.1	0.41

SEM images of photocatalysts in Figure 2 reveal the morphology of the material. The original P25 nanoparticles are uniform in size (Figure 2a). As shown in Figure 2b, images of S/TO showed the presence of hexagonal crystals with clear contours and smooth surfaces. This suggested the formation of a hybrid composition of  $\text{SrTiO}_3$  and P25 after hydrothermal treatment. Figure 2c shows that the addition of La transformed the material from hexagonal crystals to a massive structure. This may be due to the fact that the addition of La disrupts the crystal structure of  $\text{SrTiO}_3$ , causing the hexagonal crystals to be gradually transformed into a monoclinic crystal system. Moreover, Figure 2d is the morphology of La-S(T-Fe)/TO. It is obvious that the addition of Fe transformed the catalyst further from a particulate structure to a more fibrous one. Figure 2b,c shows the photocatalysts with a relatively wide distribution of particle sizes. Studies have suggested that differences in surface energy between particles of varying sizes result in varying adsorption forces, causing agglomeration [33]. Meanwhile, the adsorption isotherms of the Supplementary Material Figure S2 show that it conforms to the theoretical pore structure of the BET H3-type hysteresis loop. This results in the aggregation of laminar structures and the formation of a large number of irregular pores, slits, gullies, and other morphologies [34]. These are the reasons for the agglomeration of photocatalysts. However, the photocatalysts used in the experiments underwent ultrasonic dispersion treatment to disperse the particles as much as possible.

Figure 3 displays the UV-vis DRS analysis of the catalyst. Figure 3a demonstrates that the inclusion of metal ions leads to a substantial redshift in light absorption. The modified S/TO exhibited stronger visible light absorption at around 640 nm, and the redshift phenomenon suggests that it broadened the photoresponsivity range. Therefore, the visible light-responsive catalyst overcomes the disadvantage of a broad bandgap to some extent. Figure 3b displays the  $(\alpha h \nu)^2$  curve computed from the absorbance values, indicating that the band gap width of the catalyst diminishes with metal doping, transitioning from 3.32 eV to 3.15 eV, thus improving its ability to absorb visible light. Furthermore, the addition of La and Fe elements reduces the band gap of  $\text{SrTiO}_3$ , allowing for the absorption of a wider range of visible light wavelengths [35]. This leads to an increase in photogenerated electron holes and ultimately improves photocatalytic activity.

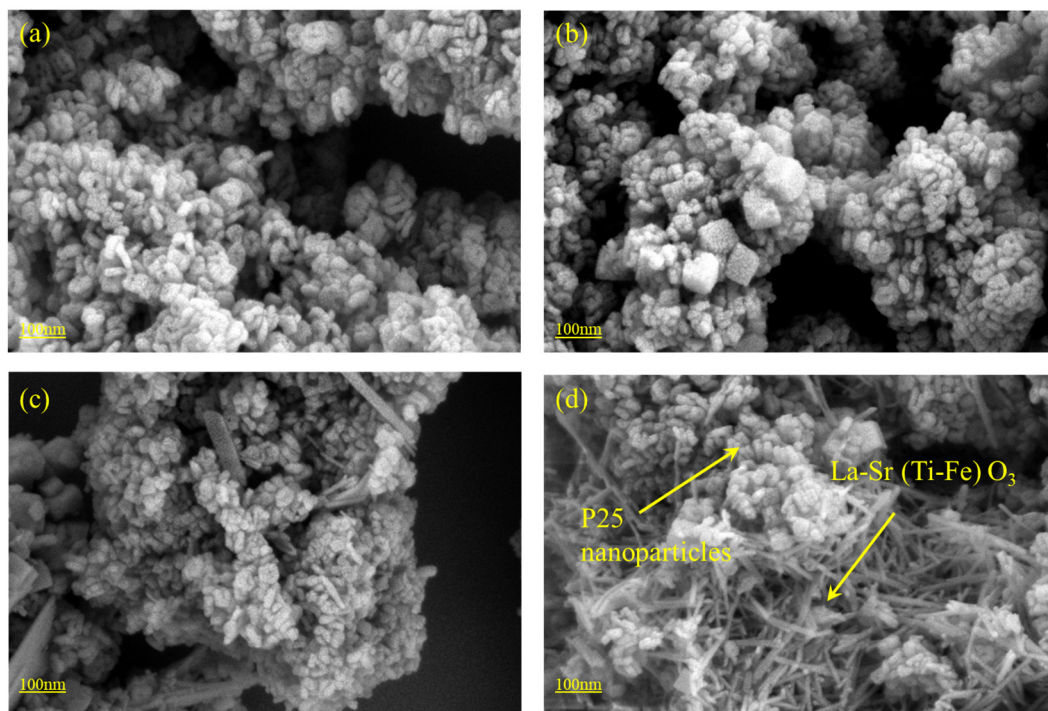


**Figure 2.** SEM Images of Catalysts: (a) P25, (b) S/TO, (c) La-S/TO, (d) La-S(T-Fe)/TO.

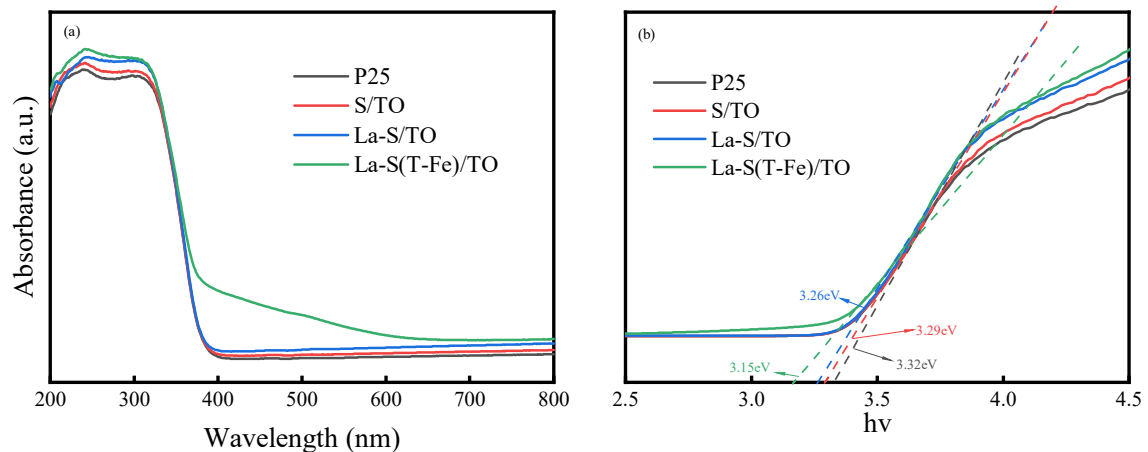


**Figure 3.** UV-vis absorption spectra of catalysts (a) diffuse reflection spectroscopy and (b) bandgaps.

The PL intensity is inversely related to the ease of electron–hole pair separation. Figure 4 displays the fluorescence spectra of the composites. The PL intensity of the S/TO composites is much lower than that of P25, indicating that the SrTiO<sub>3</sub> composite with P25 improves electron and hole separation, which lowers the likelihood of recombination. The PL intensity of the material was further weakened with the doping of La and Fe into S/TO, which caused lattice defects. The introduction of La and Fe into S/TO results in lattice defects that reduce the material’s concentration intensity. The decrease in luminescence intensity and increase in photocatalytic efficiency can be attributed to lattice defects caused by the different molecular weights of La<sup>3+</sup> and Sr<sup>3+</sup>. XRD analysis confirms this explanation. These defects create shallow potential trapping sites for photogenerated electrons and holes [36], suppressing their recombination.

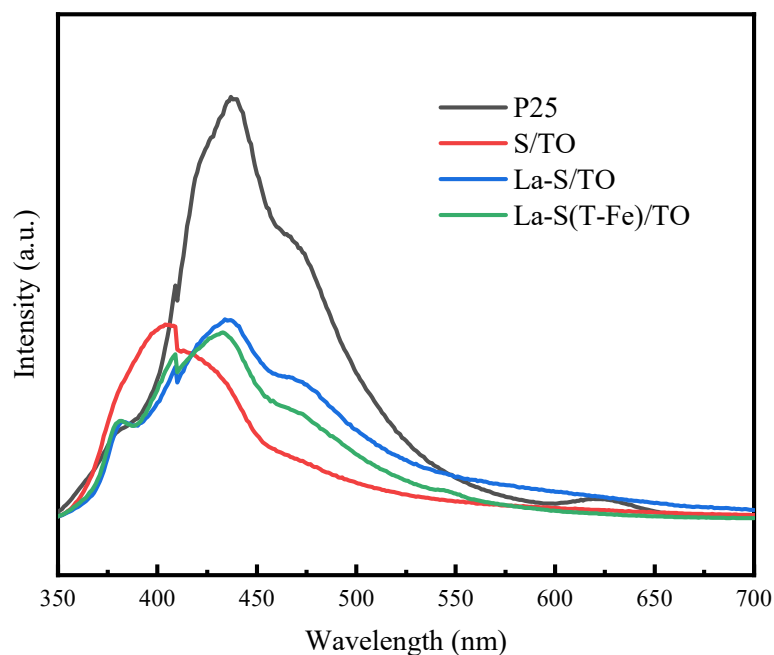


**Figure 4.** Photoluminescence spectra of different photocatalysts.

XPS spectrum of the La-S(T-Fe)/TO composite material was next obtained and is shown in Figure 5. The XPS analysis of La-S(T-Fe)/TO reveals the presence of Ti, C, Sr, La, and Fe in the material. Figure 5b displays the C 1s spectrum, indicating characteristic peaks located at 284.8 eV and 288.5 eV, identified as belonging to adventitious carbon species [37]. The data were corrected with the 284.8 eV peak. Figure 5c depicts the XPS spectrum of Ti 2p, revealing twin peaks Ti 2p<sub>3/2</sub> and Ti 2p<sub>1/2</sub>, deconvoluted into two sub-peaks, which signify the characteristic peaks of Ti<sup>3+</sup> and Ti<sup>4+</sup>. Lastly, Figure 5d illustrates the Sr 3d spectrum, including Sr 3d<sub>5/2</sub> (132.74 eV) and Sr 3d<sub>3/2</sub> (134.47 eV). The 132.74 eV peak corresponds to SrTiO<sub>3</sub>, whereas the 134.47 eV peak corresponds to the strontium oxide mixture [38]. Figure 5e displays the spectral composition of La 3d, which comprises of two double peaks, La 3d<sub>5/2</sub> and La 3d<sub>3/2</sub>, with binding energies of 834.55 and 851.40 eV, respectively. This characteristic peak of La<sup>3+</sup> indicates that La replaces part of Sr, consistent with the observed XRD pattern of La-S/T-FeO composite material. The presence of two double peaks in La, with a separation  $\Delta E$  greater than 4.0 eV, suggests that La might have been doped into the lattice as a metal element, while the remaining amount might exist as an oxide layer on the S/TO surface. Figure 5f depicts the spectrum of Fe 2p, with the core levels of Fe 2p<sub>3/2</sub> and Fe 2p<sub>1/2</sub> being the characteristic peaks that are noticeably visible in the spectrum. This observation indicates that both La and Fe elements have been successfully incorporated into the S/TO catalyst.

### 3.2. Degradation Performance of Tetracycline by Photocatalysts

Based on the material characterization, it is evident that doping metallic elements in SrTiO<sub>3</sub>/TiO<sub>2</sub> causes lattice distortion, resulting in the formation of low-potential traps for photogenerated electrons and holes. It increases the active sites of the material, reduces the bandgap width, broadens the spectral response range, and enhances the degradation efficiency of tetracycline. The removal ability of tetracycline was evaluated by testing four photocatalytic materials under visible light (Figure 6). The concentration of tetracycline did not change when no catalyst was added, indicating its stability. For this situation where the catalyst was added, a drop in tetracycline concentration was observed at the first 10 min. The concentration stabilized at 30 min. The lowering tetracycline concentration could be attributed to adsorption by catalyst materials at first [39]. The La-Sr(T-Fe)/TO composites and P25 were found to have specific surface areas of roughly 62.1 and 50.0 m<sup>2</sup>/g, respectively (Table 1). Therefore, La-Sr(T-Fe)/TO manifested a stronger adsorption

capacity under dark conditions (Figure 6). According to the results of the dark stage, a dark stage reaction time of 30 min was decided upon for all tests afterwards. The addition of catalysts greatly improved the degradation of tetracycline with visible light as a light source. There was a significant decrease in the concentration of tetracycline when the mixture was illuminated. Moreover, it was shown that the metal-doped photocatalyst had a notably greater catalytic efficacy than the undoped materials. After 120 min of illumination, P25 degraded only 57.4% of the tetracycline. In contrast, 69.1% was degraded via S/TO. La-S/TO demonstrated an even better removal efficiency of 80.7%. Notably, La-Sr(T-Fe)/TO displayed the most impressive outcome, with the degradation efficiency for tetracycline reaching 98.2% after 120 min of illumination. This suggests that a heterojunction is formed between La-Sr(T-Fe)O<sub>3</sub> and P25 through bimetallic doping, which can provide additional active sites and improve photocatalytic efficiency.

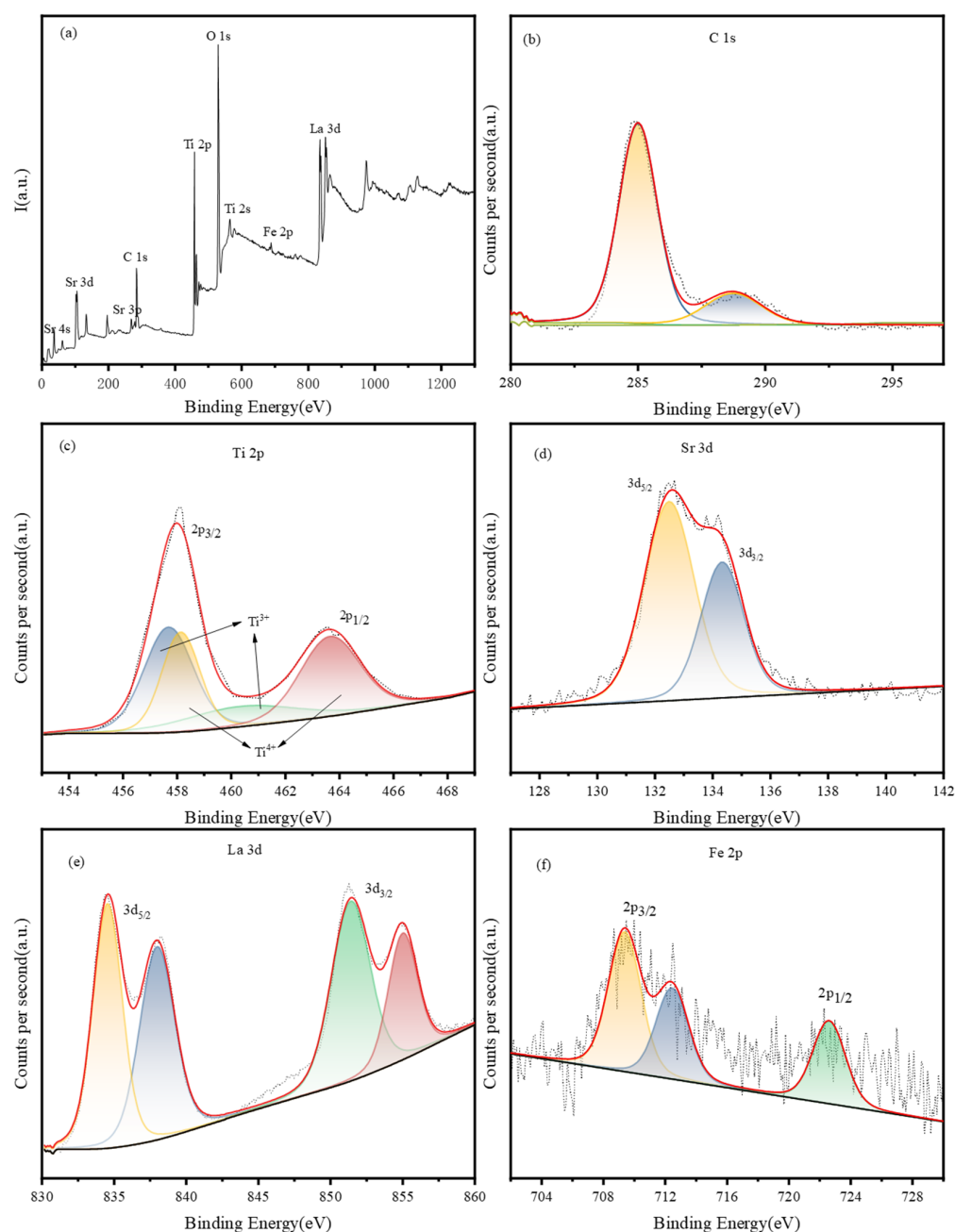
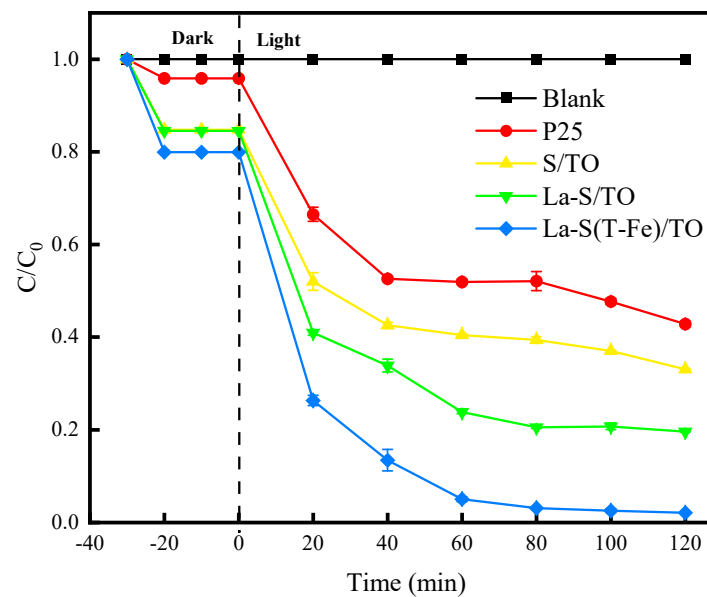


Figure 5. XPS Spectrum: (a) La-S(T-Fe)/TO, (b) C 1s, (c) Ti 2p, (d) Sr 3d, (e) La 3d and (f) Fe 2p.



**Figure 6.** Photocatalytic properties of materials. Experimental conditions:  $C_i = 30$  mg/L,  $C_c = 0.8$  g/L, pH = 6,  $T = 298$  K. ( $C_i$  is the initial concentration of tetracycline and  $C_c$  is catalyst dosages.).

### 3.3. Factors Influencing the Photocatalytic Degradation of Tetracycline

Research has demonstrated that many factors may impact the degradation capacity of photocatalytic materials on tetracycline [40]. Catalyst dosing, initial concentration, initial pH and co-existing ions and humic acid on photocatalytic division of tetracycline were investigated in detail. Figure 7a shows the variation of tetracycline removal with the catalyst dosage. At the beginning, the tetracycline concentration was 30 mg/L, and the pH of the solution was 6.0. The dose was between 0.8 and 1.6 g/L. The rate at which tetracycline degraded rose from 59.4% to 99.1% in 120 min. The higher the dosage, the larger the number of active sites and reactive species. Thus, higher dosage led to a higher number of photocatalytic reactions [41,42]. Thus, the rate at which tetracycline is degraded is enhanced. In addition, the increase in degradation ability levelled off as the dosage rose from 1.6 g/L to 2.0 g/L. It seems that a dosage of 1.6 g/L was sufficient. An excessively high dosage may cause the solution to become more turbid, which could reduce the light absorption efficiency of the catalyst. In summary, the dosage of the catalyst has an impact on the photocatalytic performance of tetracycline, and the most suitable dose is 1.6 g/L.

Figure 7b demonstrates the photocatalytic breakdown of tetracycline at varying initial concentrations. The catalyst dose was set at 1.6 g/L with an initial pH of 6.0. Degradation of tetracycline reached 99.1% after 120 min of the reaction at an initial concentration of 20 mg/L. In contrast, the degradation efficiency decreases to 61.1% at a concentration of 60 mg/L. The efficiency of degradation declined with increasing initial concentration. As the initial concentration increased, the efficiency of degradation decreased. This is because the catalyst's photocatalytic reaction sites may prove insufficient to treat tetracycline effectively, especially at higher initial concentrations. The accumulation of intermediate products could also interfere with the active substances within the system, resulting in a decreased efficiency of tetracycline degradation [43].

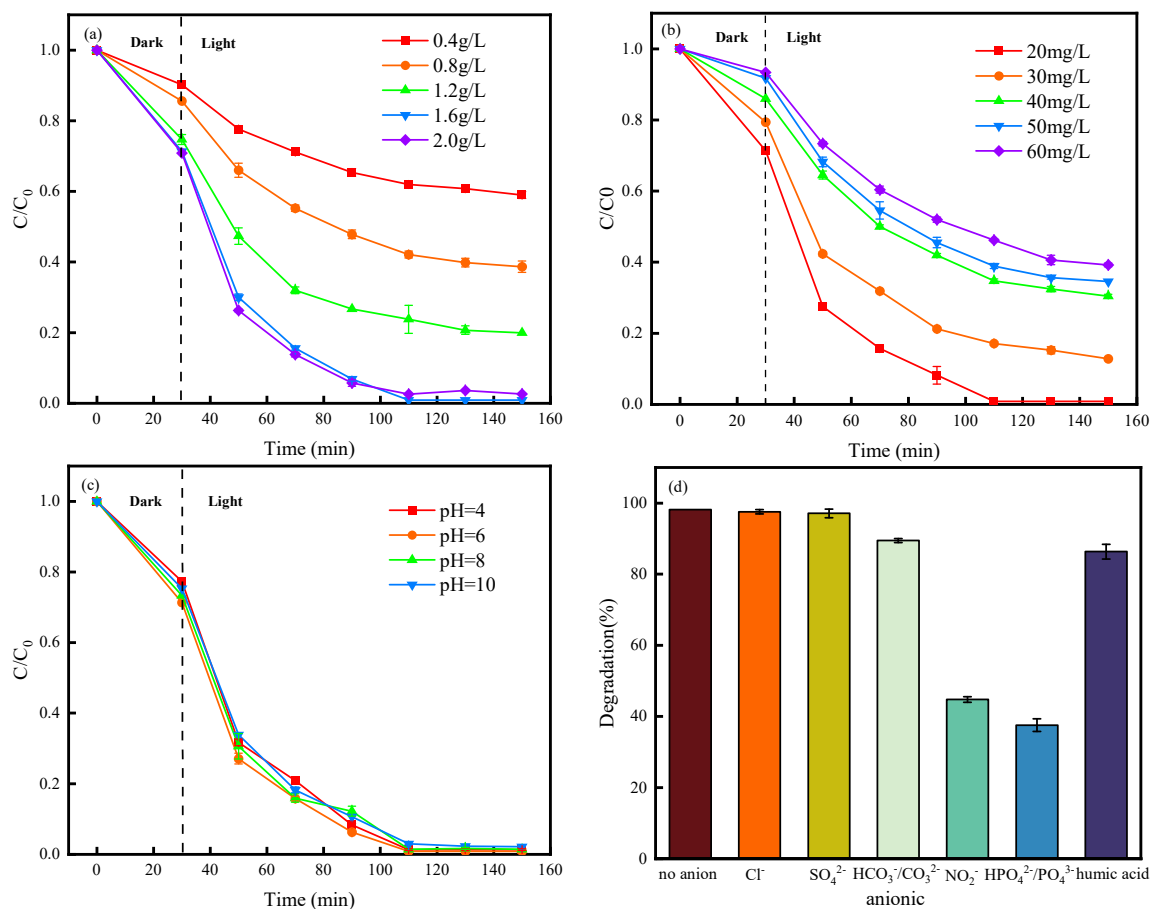


**Figure 7.** The impacts of factors on the photocatalytic degradation of tetracycline over La-Sr(T-Fe)/TO: (a) catalyst dosages; (b) initial concentrations of tetracycline; (c) initial pH values; (d) coexisting ions.

Figure 7c illustrates the change in the degradation rate of tetracycline over time in different initial pH conditions. The initial tetracycline concentration and catalyst dosage were set at 20 mg/L and 1.6 g/L, respectively. The pH level influences the surface charges of the photocatalyst and the forms of organic compounds, which subsequently affects the photocatalyst's adsorption capacity for the target pollutant. Notwithstanding, the trial outcomes propose that La-Sr(T-Fe)/TO displays a considerable level of tolerance towards fluctuations in pH. The rate of tetracycline degradation shows little variation within the pH range of 4–10. To explore this phenomenon, pH measurements were taken at different intervals during the experiment. It was observed that the pH of the filtered samples underwent continuous fluctuations before eventually stabilizing around 5.0. It can be concluded that tetracycline degradation occurs under similar pH conditions and is not significantly influenced by the initial pH levels. This elucidates why the degradation rate of tetracycline remains relatively constant across varying initial pH conditions. Furthermore, upon completion of the photocatalytic experiments, the filtered solution underwent testing for iron leaching. The results indicated that a certain amount of  $\text{Fe}^{3+}$  was detected at lower pH values. However, at pH values greater than 6, there was no detectable iron leaching from the solution.

The presence of multiple substances in aquaculture wastewater is a significant factor that affects photocatalytic reactions. It is imperative to consider these factors for effective photocatalytic reactions. Figure 7d demonstrates how coexisting anions ( $\text{Cl}^-$ ,  $\text{SO}_4^{2-}$ ,  $\text{CO}_3^{2-}/\text{HCO}_3^-$ ,  $\text{NO}_2^-$ ,  $\text{HPO}_4^{2-}/\text{PO}_4^{3-}$ ) and humic acid can influence the photocatalytic efficiency in tetracycline solution. In comparison to the photocatalytic degradation efficacy without the inclusion of anions, the presence of  $\text{Cl}^-$ ,  $\text{SO}_4^{2-}$ , and  $\text{CO}_3^{2-}/\text{HCO}_3^-$  has a minimal effect on the photocatalytic reaction system. Conversely,  $\text{NO}_2^-$  and  $\text{HPO}_4^{2-}/\text{PO}_4^{3-}$

have an adverse impact on the photocatalytic reaction of tetracycline due to their observed scavenging effect on  $\bullet\text{OH}$  and holes [44]. Furthermore, contaminant molecules and contained anions compete for the active sites on the catalyst surface [45].  $\text{HPO}_4^{2-}/\text{PO}_4^{3-}$  transform  $\bullet\text{OH}$  to  $\text{OH}^-$ , thereby inhibiting the degradation of tetracycline. Consequently, when addressing tetracycline in photocatalysis for high-nitrogen and high-phosphorus wastewater, it is imperative to take into account the impact of nitrogen and phosphorus on the photo reaction system. Simultaneously, the presence of humic acid also impacts the degradation of tetracycline. At 30 mg/L of humic acid, it decreased from 99.1% to 86.9%. This decrease is a result of humic acid, which competes with tetracycline for active substances.

### 3.4. Stability Experiment

The reusability of photocatalytic materials is a crucial factor in evaluating photocatalyst performance. Figure 8 displays the results of cycling experiments conducted on La-S(T-Fe)/TO. The composite for the rate of tetracycline degradation remained somewhat stable in the following three cycles despite a slight decline in the photocatalytic degradation efficiency of the drug following the second cycle. The decrease in the rate of degradation may be due to the loss of a small amount of catalyst during the recycling process, as well as a reduction in adsorption sites on the catalyst. The cycling experiment showed that the stability of the material decreased to some extent, but the material still had a good degradation rate of tetracycline after several cycles.

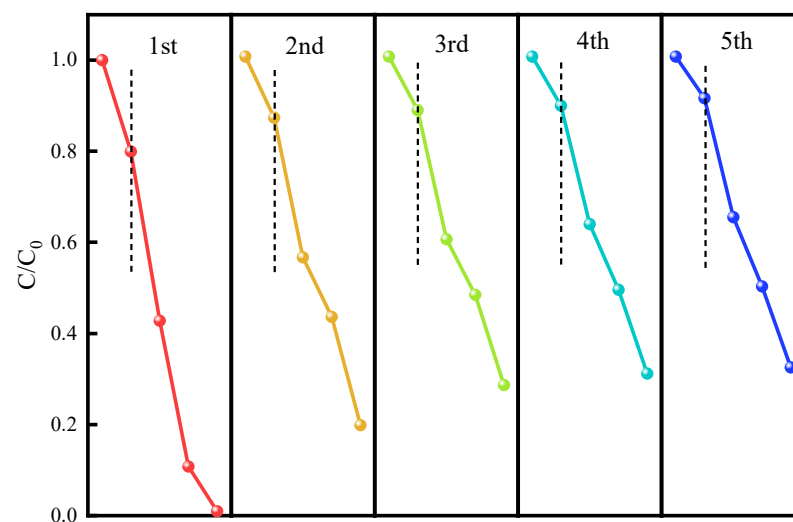


**Figure 8.** Cyclic stability of La-S(T-Fe)/TO degraded tetracycline.

### 3.5. Radical Quenching and Photocatalytic Mechanism

Figure 9a displays the results of the radical quenching experiment. It indicates that in the light-catalyzed reaction with BQ involved in the photocatalytic degradation of tetracycline, the La-S(T-Fe)/TO composite material reduces the photocatalytic degradation rate of tetracycline by approximately 21% compared to the case without a capture agent. The addition of BQ markedly inhibits the production of  $\bullet\text{O}_2^-$ , indicating its pivotal role as the primary active species in the photocatalytic reaction. Furthermore, the photocatalytic degradation efficacy of tetracycline by La-S(T-Fe)/TO (in the presence of TEA) was approximately 70%, which suggests that  $\text{h}^+$  also contributes to the reaction mechanism. When TBA is added as an inhibitor, the removal rate of tetracycline is slightly reduced, but still maintained at a high level. This suggests that although  $\bullet\text{OH}$  participates in the photocatalytic reaction, it is not the primary active group. In summary, the order of influence of active substances is:  $\bullet\text{O}_2^- > \text{h}^+ > \bullet\text{OH}$ . Although all three types of free radicals are involved in the photocatalytic reaction,  $\bullet\text{O}_2^-$  and  $\text{h}^+$  are the primary factors.

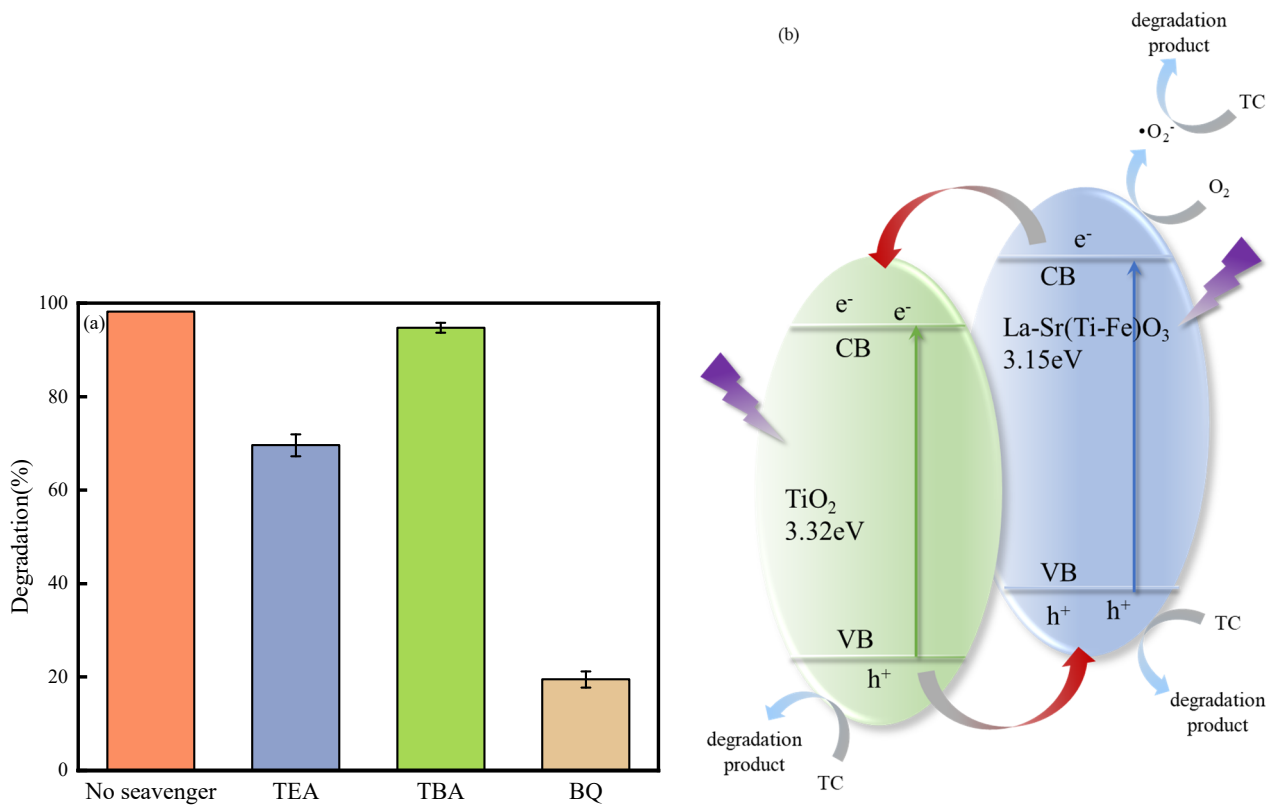


**Figure 9.** (a) Radical trapping experiments on La-S(Ti-Fe)/TO; (b) schematic diagram of photocatalytic degradation mechanism of La-S(Ti-Fe)/TO.

This study reports that the conduction band of P25 and the valence band of La-Sr (Ti-Fe) O<sub>3</sub> are 2.76 eV [46] and 2.45 eV [32,47], respectively. As shown in Figure 3, the bandgap of P25 is 3.32 eV compared to 3.15 eV for the metal-doped material. Equation (1) can be used to determine the valence bands [48]:

$$E_{VB} = E_{CB} + E_g \quad (1)$$

The results showed that the conduction bands of P25 and La-Sr (Ti-Fe) O<sub>3</sub> were  $-0.56$  and  $-0.7$  eV, respectively. From the experimental and characterization results presented above, it is possible to propose a Type-II heterojunction photocatalytic degradation mechanism diagram for La-S(Ti-Fe)/TO composites (Figure 9b). Notably, the CB edge of La-Sr (Ti-Fe) O<sub>3</sub> is higher than P25 and the VB of P25 is lower than that of La-Sr (Ti-Fe) O<sub>3</sub>, which means that the band gap position and structure of La-S(Ti-Fe)/TO belong to the traditional Type-II heterojunction structure and this could accelerate the transmission of photogenerated carriers [49]. Under visible light irradiation, P25 and La-Sr (Ti-Fe) O<sub>3</sub> are excited. It illustrates electrons on the CB of La-Sr (Ti-Fe) O<sub>3</sub> transition gradually to the CB of P25. Simultaneously, photogenerated holes on the VB of P25 flow through the La-S(Ti-Fe)/TiO<sub>2</sub> composite material to the VB of La-Sr (Ti-Fe) O<sub>3</sub>. This migration causes separation between electrons and photogenerated holes, forming shallow potential trapping sites. As a result, the photocatalytic efficiency enhances. This is in line with the analysis findings of the UV-vis DRS and photoluminescence (PL) spectra of the catalyst. Thus, in order to perform photocatalysis, the electrons confined to the oxygen-deficient sites positively contribute to the synthesis of •O<sub>2</sub><sup>-</sup>, which, in turn, transforms tetracycline into small, non-toxic molecules. The holes generated from the valence band will disintegrate the tetracycline pollutant directly, creating the production of a limited quantity of •OH for the oxidation of tetracycline.

### 3.6. Degradation Pathways of Tetracycline

Aqueous samples from the tetracycline degradation process via the La-S(T-Fe)/TO photocatalyst were analyzed for intermediates using HPLC-MS. A total of 12 intermediates were identified, including  $C_{22}H_{24}N_2O_{10}$  ( $m/z = 497$ ),  $C_{19}H_{18}N_2O_8$  ( $m/z = 402$ ), and  $C_{14}H_8O_{10}$  ( $m/z = 354$ ). Figure S2 displays the results, which indicate three possible degradation pathways [50–52]. Pathway I entails eliminating three methyl groups from tetracycline, resulting in the intermediate with an  $m/z$  of 402. Subsequently, the intermediate undergoes a series of reactions, including deamination, dihydroxylation, deamidation, ring-opening, and carbonylation, leading to the intermediate with an  $m/z$  of 354. The enol structure of the  $m/z = 354$  intermediate is unstable and undergoes rapid conversion into a ketone structure, producing products with  $m/z = 249$  and  $m/z = 174$ . In Pathway II, tetracycline undergoes hydroxylation to produce a product  $m/z = 372$ . Subsequently, it undergoes demethylation and C-C bond cleavage, forming an intermediate with a mass-to-charge ratio of 178. In Pathway III, tetracycline undergoes several hydroxylation and oxidation reactions, leading to the formation of an intermediate with  $m/z = 497$ . It then undergoes ring-opening and dehydroxylation to yield two other intermediates with  $m/z = 339$  and  $m/z = 178$ , respectively. Next, the intermediates undergo double bond cleavage and further ring-opening reactions, forming smaller molecules with  $m/z = 112$  and  $m/z = 113$ . Ultimately, all three pathways result in the production of small molecules such as  $CO_2$  and  $H_2O$ .

## 4. Conclusions

The doping of metal elements in  $SrTiO_3/TiO_2$  results in lattice distortion, creating shallow potential traps for photogenerated electrons and holes. This increases photocatalytic activity, decreases band gap width, widens the spectral response range, and boosts tetracycline degradation efficiency. The study found that within the La and Fe-doped La-S(Ti-Fe)/TO double-metal system, the most significant effect occurred. This resulted in a degradation rate of 99.1% after 120 min of visible light irradiation when the initial tetracycline concentration was 20 mg/L. Additionally, the investigation into coexisting ions and humic acid displayed that  $NO_2^-$  and  $HPO_4^{2-}/PO_4^{3-}$  exhibit a substantial inhibitory effect, whereas the influence of humic acid is rather limited. There was no discernible variation in the effectiveness of photocatalytic tetracycline degradation throughout a broad starting pH range. Even after five cycling experiments, the photocatalyst continued to exhibit good photocatalytic performance. Ultimately, tetracycline underwent a gradual transformation into small molecules and was eventually converted into water and carbon dioxide via the impact of the active substance. This study enhances the composition structure, photoelectric properties, and photocatalytic functionality of metal-doped  $SrTiO_3/TiO_2$ . However, this study investigated only the double metal-doped photocatalyst's ability to degrade organics with tetracycline as representative. The effectiveness of this catalyst for other commonly found pollutants, such as in aquaculture wastewater, needs further exploration.

**Supplementary Materials:** The following supporting information can be downloaded at: <https://www.mdpi.com/article/10.3390/w16020210/s1>, Figure S1: Nitrogen physisorption isotherm and pore size distribution (inset) of La-S(Ti-Fe)/TO; Figure S2. degradation pathway of tetracycline by La-S(T-Fe)/TO.

**Author Contributions:** Investigation, M.H.; data curation, M.H.; writing—original draft, M.H. and W.C.; writing—review and editing, M.H., W.C. and J.W.; supervision, J.W.; project administration, J.W.; Funding acquisition, J.W. All authors have read and agreed to the published version of the manuscript.

**Funding:** This work was supported by the Natural Science Foundation of Shanghai (No. 21ZR1479900) and Central Public-interest Scientific Institution Basal Research Fund, CAFS (No. 2023CG03).

**Data Availability Statement:** The data presented in this study are available upon request from the corresponding author.

**Conflicts of Interest:** The authors declare no conflicts of interest. The funders had no role in the design of the study; in the collection, analyses, or interpretation of data; in the writing of the manuscript; or in the decision to publish the results.

## References

1. Kafaei, R.; Papari, F.; Seyedabadi, M.; Sahebi, S.; Tahmasebi, R.; Ahmadi, M.; Sorial, G.A.; Asgari, G.; Ramavandi, B. Occurrence, distribution, and potential sources of antibiotics pollution in the water-sediment of the northern coastline of the Persian Gulf, Iran. *Sci. Total Environ.* **2018**, *627*, 703–712. [[CrossRef](#)] [[PubMed](#)]
2. Wammer, K.H.; Slattery, M.T.; Stemig, A.M.; Ditty, J.L. Tetracycline photolysis in natural waters: Loss of antibacterial activity. *Chemosphere* **2011**, *85*, 1505–1510. [[CrossRef](#)] [[PubMed](#)]
3. Chen, T.; Luo, L.; Deng, S.; Shi, G.; Zhang, S.; Zhang, Y.; Deng, O.; Wang, L.; Zhang, J.; Wei, L. Sorption of tetracycline on H<sub>3</sub>PO<sub>4</sub> modified biochar derived from rice straw and swine manure. *Bioresour. Technol.* **2018**, *267*, 431–437. [[CrossRef](#)] [[PubMed](#)]
4. Yu, F.; Li, Y.; Han, S.; Ma, J. Adsorptive removal of antibiotics from aqueous solution using carbon materials. *Chemosphere* **2016**, *153*, 365–385. [[CrossRef](#)] [[PubMed](#)]
5. Zhu, X.-D.; Wang, Y.-J.; Sun, R.-J.; Zhou, D.-M. Photocatalytic degradation of tetracycline in aqueous solution by nanosized TiO<sub>2</sub>. *Chemosphere* **2013**, *92*, 925–932. [[CrossRef](#)] [[PubMed](#)]
6. Qi, N.; Wang, P.; Wang, C.; Ao, Y. Effect of a typical antibiotic (tetracycline) on the aggregation of TiO<sub>2</sub> nanoparticles in an aquatic environment. *J. Hazard. Mater.* **2018**, *341*, 187–197. [[CrossRef](#)] [[PubMed](#)]
7. Silva, C.P.; Louros, V.; Silva, V.; Otero, M.; Lima, D.L.D. Antibiotics in Aquaculture Wastewater: Is It Feasible to Use a Photodegradation-Based Treatment for Their Removal? *Toxics* **2021**, *9*, 194. [[CrossRef](#)]
8. Iakovides, I.C.; Michael-Kordatou, I.; Moreira, N.F.F.; Ribeiro, A.R.; Fernandes, T.; Pereira, M.F.R.; Nunes, O.C.; Manaia, C.M.; Silva, A.M.T.; Fatta-Kassinos, D. Continuous ozonation of urban wastewater: Removal of antibiotics, antibiotic-resistant *Escherichia coli* and antibiotic resistance genes and phytotoxicity. *Water Res.* **2019**, *159*, 333–347. [[CrossRef](#)]
9. Wang, Y.; Zhang, H.; Zhang, J.; Lu, C.; Huang, Q.; Wu, J.; Liu, F. Degradation of tetracycline in aqueous media by ozonation in an internal loop-lift reactor. *J. Hazard. Mater.* **2011**, *192*, 35–43. [[CrossRef](#)]
10. Xu, B.L.; Liu, F.; Brookes, P.C.; Xu, J.M. Microplastics play a minor role in tetracycline sorption in the presence of dissolved organic matter. *Environ. Pollut.* **2018**, *240*, 87–94. [[CrossRef](#)]
11. Hosseini-Bandegharai, A.; Alahabadi, A.; Rahmani-Sani, A.; Rastegar, A.; Khamirchi, R.; Mehrpouyan, M.; Agah, J.; Pajohankia, Z. Effect of nitrate and amine functionalization on the adsorption properties of a macroporous resin towards tetracycline antibiotic. *J. Taiwan Inst. Chem. Eng.* **2016**, *66*, 143–153. [[CrossRef](#)]
12. Liu, K.; Chen, J.F.; Sun, F.F.; Liu, Y.Y.; Tang, M.Z.; Yang, Y.W. Historical development and prospect of intimately coupling photocatalysis and biological technology for pollutant treatment in sewage: A review. *Sci. Total Environ.* **2022**, *835*, 155482. [[CrossRef](#)] [[PubMed](#)]
13. Akhundi, A.; Badiei, A.; Ziarani, G.M.; Habibi-Yangjeh, A.; Muñoz-Batista, M.J.; Luque, R. Graphitic carbon nitride-based photocatalysts: Toward efficient organic transformation for value-added chemicals production. *Mol. Catal.* **2020**, *488*, 110902. [[CrossRef](#)]
14. Akhundi, A.; Habibi-Yangjeh, A.; Abitorabi, M.; Pouran, S.R. Review on photocatalytic conversion of carbon dioxide to value-added compounds and renewable fuels by graphitic carbon nitride-based photocatalysts. *Catal. Rev.-Sci. Eng.* **2019**, *61*, 595–628. [[CrossRef](#)]
15. Shekofteh-Gohari, M.; Habibi-Yangjeh, A.; Abitorabi, M.; Rouhi, A. Magnetically separable nanocomposites based on ZnO and their applications in photocatalytic processes: A review. *Crit. Rev. Environ. Sci. Technol.* **2018**, *48*, 806–857. [[CrossRef](#)]
16. Zhang, L.; Xiao, P.; Che, B.; Yang, J.; Cai, Z.; Wang, H.; Gao, J.; Liang, W.; Wu, C.; Chen, T.J.C. Mechanistic Study of the Transition from Antimony Oxide to Antimony Sulfide in the Hydrothermal Process to Obtain Highly Efficient Solar Cells. *Environmental Prog. Sustain. Energy* **2023**, *16*, e202202049. [[CrossRef](#)] [[PubMed](#)]
17. Yanagida, S.; Sano, K.; Takei, T.; Kumada, N. Preparation and photocatalytic properties of rutile TiO<sub>2</sub> with a unique morphology and SrTiO<sub>3</sub>-TiO<sub>2</sub> composites obtained by acid treatment of SrTiO<sub>3</sub>. *Mater. Res. Bull.* **2020**, *125*, 110762. [[CrossRef](#)]
18. Cao, T.; Li, Y.; Wang, C.; Shao, C.; Liu, Y. A Facile in Situ Hydrothermal Method to SrTiO<sub>3</sub>/TiO<sub>2</sub> Nanofiber Heterostructures with High Photocatalytic Activity. *Langmuir* **2011**, *27*, 2946–2952. [[CrossRef](#)]
19. Wei, Y.; Wang, J.; Yu, R.; Wan, J.; Wang, D. Constructing SrTiO<sub>3</sub>-TiO<sub>2</sub> Heterogeneous Hollow Multi-shelled Structures for Enhanced Solar Water Splitting. *Angew Chem. Int. Ed. Engl.* **2019**, *58*, 1422–1426. [[CrossRef](#)]
20. Karacasulu, L.; Kartal, U.; Icin, O.; Bortolotti, M.; Biesuz, M.; Vakifahmetoglu, C. Formation of monolithic SrTiO<sub>3</sub>-TiO<sub>2</sub> ceramic heterostructures by reactive hydrothermal sintering. *J. Eur. Ceram. Soc.* **2023**, *43*, 6982–6988. [[CrossRef](#)]
21. Guo, Y.H.; Zhou, S.H.; Sun, X.K.; Yuan, H.L. Improving photocatalytic activity in NO removal by adding metallic bismuth to SrTiO<sub>3</sub> nanoparticles. *Ceram. Int.* **2020**, *46*, 14257–14261. [[CrossRef](#)]
22. Hirayama, J.; Abe, R.; Kamiya, Y. Combinational effect of Pt/SrTiO<sub>3</sub>:Rh photocatalyst and SnPd/Al<sub>2</sub>O<sub>3</sub> non-photocatalyst for photocatalytic reduction of nitrate to nitrogen in water under visible light irradiation. *Appl. Catal. B-Environ.* **2014**, *144*, 721–729. [[CrossRef](#)]
23. Liu, Z.D.; Ma, Z. Ag-SrTiO<sub>3</sub>/TiO<sub>2</sub> composite nanostructures with enhanced photocatalytic activity. *Mater. Res. Bull.* **2019**, *118*, 110492. [[CrossRef](#)]

24. Lucas, T.T.A.; Melo, M.A.; Freitas, A.L.M.; Souza, F.L.; Goncalves, R.V. Enhancing the solar water splitting activity of TiO<sub>2</sub> nanotube-array photoanode by surface coating with La-doped SrTiO<sub>3</sub>. *Sol. Energy Mater. Sol. Cells* **2020**, *208*, 110428. [[CrossRef](#)]
25. Srivastava, D.; Norman, C.; Azough, F.; Schäfer, M.C.; Guilmeau, E.; Kepaptsoglou, D.; Ramasse, Q.M.; Nicotra, G.; Freer, R.J.P.C.C.P. Tuning the thermoelectric properties of A-site deficient SrTiO<sub>3</sub> ceramics by vacancies and carrier concentration. *Phys. Chem. Chem. Phys.* **2016**, *18*, 26475–26486. [[CrossRef](#)]
26. Vračar, M.; Kuzmin, A.; Merkle, R.; Purans, J.; Kotomin, E.; Maier, J.; Mathon, O. Jahn-Teller distortion around Fe<sup>4+</sup> in Sr (Fe<sub>x</sub>Ti<sub>1-x</sub>) O<sub>3-δ</sub> from X-ray absorption spectroscopy, X-ray diffraction, and vibrational spectroscopy. *Phys. Rev. B* **2007**, *76*, 174107. [[CrossRef](#)]
27. da Silva, L.; Bernardi, M.; Maia, L.; Frigo, G.; Mastelaro, V. Synthesis and thermal decomposition of SrTi<sub>1-x</sub>Fe<sub>x</sub>O<sub>3</sub> (0.0 a parts per thousand currency sign xa parts per thousand currency sign 0.1) powders obtained by the polymeric precursor method. *J. Therm. Anal. Calorim.* **2009**, *97*, 173–177. [[CrossRef](#)]
28. Kayaalp, B.; Lee, S.; Klauke, K.; Seo, J.; Nodari, L.; Kornowski, A.; Jung, W.; Mascotto, S. Template-free mesoporous La<sub>0.3</sub>Sr<sub>0.7</sub>Ti<sub>1-x</sub>Fe<sub>x</sub>O<sub>3±δ</sub> for CH<sub>4</sub> and CO oxidation catalysis. *Appl. Catal. B Environ.* **2019**, *245*, 536–545. [[CrossRef](#)]
29. Guo, R.; Fang, L.; Dong, W.; Zheng, F.; Shen, M. Enhanced photocatalytic activity and ferromagnetism in Gd doped BiFeO<sub>3</sub> nanoparticles. *J. Phys. Chem. C* **2010**, *114*, 21390–21396. [[CrossRef](#)]
30. Janotti, A.; Jalan, B.; Stemmer, S.; Van de Walle, C.G. Effects of doping on the lattice parameter of SrTiO<sub>3</sub>. *Appl. Phys. Lett.* **2012**, *100*, 262104. [[CrossRef](#)]
31. Xu, Q.; Zhu, B.; Jiang, C.; Cheng, B.; Yu, J. Constructing 2D/2D Fe<sub>2</sub>O<sub>3</sub>/g-C<sub>3</sub>N<sub>4</sub> direct Z-scheme photocatalysts with enhanced H<sub>2</sub> generation performance. *Sol. Rrl.* **2018**, *2*, 1800006. [[CrossRef](#)]
32. Suwannaruang, T.; Pratyauwat, A.; Sinthujariwat, P.; Wantala, K.; Chirawatkul, P.; Junlek, N.; Nijpanich, S.; Shahmoradi, B.; Shivaraju, H.P. Dynamically driven perovskite La-Fe-modified SrTiO<sub>3</sub> nanocubes and their improved photoresponsive activity under visible light: Influence of alkaline environment. *Environ. Sci. Pollut. Res.* **2023**, *30*, 90298–90317. [[CrossRef](#)] [[PubMed](#)]
33. Yokota, Y.; Horii, S.; Ogino, H.; Yoshida, Y.; Yoshikawa, A. Microstructure and thermoelectric properties of La-doped SrTiO<sub>3</sub>/TiO<sub>2</sub> eutectic crystals grown by Micro-Pulling-Down method. *J. Cryst. Growth* **2022**, *583*, 126551. [[CrossRef](#)]
34. Sun, H.; Dong, C.L.; Huang, A.J.; Zhan, H.J.; Wang, G.; Liu, W.Y.; Ma, B.J.; Wang, W. Transition Metal Doping Induces Ti<sup>3+</sup> to Promote the Performance of SrTiO<sub>3</sub>@TiO<sub>2</sub> Visible Light Photocatalytic Reduction of CO<sub>2</sub> to Prepare C1 Product. *Chem.-A Eur. J.* **2022**, *28*, e202200019. [[CrossRef](#)]
35. Zhang, N.; Ciriminna, R.; Pagliaro, M.; Xu, Y.-J. Nanochemistry-derived Bi<sub>2</sub>WO<sub>6</sub> nanostructures: Towards production of sustainable chemicals and fuels induced by visible light. *Chem. Soc. Rev.* **2014**, *43*, 5276–5287. [[CrossRef](#)] [[PubMed](#)]
36. Miyauchi, M.; Takashio, M.; Tobimatsu, H. Photocatalytic Activity of SrTiO<sub>3</sub> Codoped with Nitrogen and Lanthanum under Visible Light Illumination. *Langmuir* **2004**, *20*, 232–236. [[CrossRef](#)] [[PubMed](#)]
37. Xiao, J.; Xie, Y.; Nawaz, F.; Jin, S.; Duan, F.; Li, M.; Cao, H. Super synergy between photocatalysis and ozonation using bulk g-C<sub>3</sub>N<sub>4</sub> as catalyst: A potential sunlight/O<sub>3</sub>/g-C<sub>3</sub>N<sub>4</sub> method for efficient water decontamination. *Appl. Catal. B Environ.* **2016**, *181*, 420–428. [[CrossRef](#)]
38. Wenderich, K.; Mul, G. Methods, Mechanism, and Applications of Photodeposition in Photocatalysis: A Review. *Chem. Rev.* **2016**, *116*, 14587–14619. [[CrossRef](#)]
39. Liu, H.; Huo, W.; Zhang, T.C.; Ouyang, L.; Yuan, S. Photocatalytic removal of tetracycline by a Z-scheme heterojunction of bismuth oxyiodide/exfoliated g-C<sub>3</sub>N<sub>4</sub>: Performance, mechanism, and degradation pathway. *Mater. Today Chem.* **2022**, *23*, 100729. [[CrossRef](#)]
40. Huo, B.; Meng, F.; Yang, J.; Wang, Y.; Qi, J.; Ma, W.; Wang, Z.; Wang, J.; Wang, Z. High efficiently piezocatalysis degradation of tetracycline by few-layered MoS<sub>2</sub>/GDY: Mechanism and toxicity evaluation. *Chem. Eng. J.* **2022**, *436*, 135173. [[CrossRef](#)]
41. Xu, H.; Zhang, Y.; Wang, Y.; Zhang, L.; Zhang, Z.; Zhong, L.; He, Z.; Zheng, Y.; Shen, Y. Heterojunction material BiYO<sub>3</sub>/g-C<sub>3</sub>N<sub>4</sub> modified with cellulose nanofibers for photocatalytic degradation of tetracycline. *Carbohydr. Polym.* **2023**, *312*, 120829. [[CrossRef](#)] [[PubMed](#)]
42. Cao, W.; Yuan, Y.; Yang, C.; Wu, S.; Cheng, J. In-situ fabrication of g-C<sub>3</sub>N<sub>4</sub>/MIL-68(In)-NH<sub>2</sub> heterojunction composites with enhanced visible-light photocatalytic activity for degradation of ibuprofen. *Chem. Eng. J.* **2020**, *391*, 123608. [[CrossRef](#)]
43. Chen, F.; Yang, Q.; Wang, Y.; Zhao, J.; Wang, D.; Li, X.; Guo, Z.; Wang, H.; Deng, Y.; Niu, C.; et al. Novel ternary heterojunction photocatalyst of Ag nanoparticles and g-C<sub>3</sub>N<sub>4</sub> nanosheets co-modified BiVO<sub>4</sub> for wider spectrum visible-light photocatalytic degradation of refractory pollutant. *Appl. Catal. B Environ.* **2017**, *205*, 133–147. [[CrossRef](#)]
44. Du, C.; Zhang, Z.; Tan, S.; Yu, G.; Chen, H.; Zhou, L.; Yu, L.; Su, Y.; Zhang, Y.; Deng, F.; et al. Construction of Z-scheme g-C<sub>3</sub>N<sub>4</sub>/MnO<sub>2</sub>/GO ternary photocatalyst with enhanced photodegradation ability of tetracycline hydrochloride under visible light radiation. *Environ. Res.* **2021**, *200*, 111427. [[CrossRef](#)] [[PubMed](#)]
45. Cao, J.; Yang, Z.; Xiong, W.; Zhou, Y.; Peng, Y.; Li, X.; Zhou, C.; Xu, R.; Zhang, Y. One-step synthesis of Co-doped UiO-66 nanoparticle with enhanced removal efficiency of tetracycline: Simultaneous adsorption and photocatalysis. *Chem. Eng. J.* **2018**, *353*, 126–137. [[CrossRef](#)]
46. Liu, D.H.; Zeng, M.L.; Li, Z.; Zhu, Z.Q.; Chen, Y.; Thummavichai, K.; Ola, O.; Wang, N.N.; Zhu, Y.Q. Interfacial construction of P25/Bi<sub>2</sub>WO<sub>6</sub> composites for selective CO<sub>2</sub> photoreduction to CO in gas-solid reactions. *RSC Adv.* **2023**, *13*, 8564–8576. [[CrossRef](#)] [[PubMed](#)]

47. Han, J.; Sun, Q.; Song, Y. Enhanced thermoelectric properties of La and Dy co-doped, Sr-deficient SrTiO<sub>3</sub> ceramics. *J. Alloys Compd.* **2017**, *705*, 22–27. [[CrossRef](#)]
48. Lancet, D.; Pecht, I. Spectroscopic and immunochemical studies with nitrobenzoxadiazolealanine, a fluorescent dinitrophenyl analog. *Biochemistry* **1977**, *16*, 5150–5157. [[CrossRef](#)]
49. Güy, N. Directional transfer of photocarriers on CdS/g-C<sub>3</sub>N<sub>4</sub> heterojunction modified with Pd as a cocatalyst for synergistically enhanced photocatalytic hydrogen production. *Appl. Surf. Sci.* **2020**, *522*, 146442. [[CrossRef](#)]
50. Zhang, B.; Xu, H.; Wang, M.; Su, L.; Zhang, S.; Zhang, Y.; Wang, Q. Bismuth (III)-based metal-organic framework for tetracycline removal via adsorption and visible light catalysis processes. *J. Environ. Chem. Eng.* **2022**, *10*, 108469. [[CrossRef](#)]
51. Niu, L.; Zhang, G.; Xian, G.; Ren, Z.; Wei, T.; Li, Q.; Zhang, Y.; Zou, Z. Tetracycline degradation by persulfate activated with magnetic  $\gamma$ -Fe<sub>2</sub>O<sub>3</sub>/CeO<sub>2</sub> catalyst: Performance, activation mechanism and degradation pathway. *Sep. Purif. Technol.* **2021**, *259*, 118156. [[CrossRef](#)]
52. Kuang, X.; Fu, M.; Kang, H.; Lu, P.; Bai, J.; Yang, Y.; Gao, S. A BiOIO<sub>3</sub>/BiOBr n-n heterojunction was constructed to enhance the photocatalytic degradation of TC. *Opt. Mater.* **2023**, *138*, 113690. [[CrossRef](#)]

**Disclaimer/Publisher's Note:** The statements, opinions and data contained in all publications are solely those of the individual author(s) and contributor(s) and not of MDPI and/or the editor(s). MDPI and/or the editor(s) disclaim responsibility for any injury to people or property resulting from any ideas, methods, instructions or products referred to in the content.